Magnetic field-induced emissivity tuning of InSb-based metamaterials in the terahertz frequency regime

ANDREW CARATENUTO,[1] FANGQI CHEN,[1] YANPEI TIAN,[1] MAURO ANTEZZA,[2,3] (iD) GANG XIAO,[4] AND YI ZHENG[1,5,*]

[1]*Department of Mechanical and Industrial Engineering, Northeastern University, Boston, MA 02115, USA*
[2]*Laboratoire Charles Coulomb (L2C), UMR 5221 CNRS-Université de Montpellier, F- 34095 Montpellier, France*
[3]*Institut Universitaire de France, 1 rue Descartes, F- 75231, Paris Cedex 05, France*
[4]*Department of Physics, Brown University, Providence, RI 02912, USA*
[5]*Department of Electrical and Computer Engineering, Northeastern University, Boston, MA 02115, USA*
*y.zheng@northeastern.edu

Abstract: This work demonstrates the magnetic field-induced spectral properties of metamaterials incorporating both indium antimonide (InSb) and tungsten (W) in the terahertz (THz) frequency regime. Nanostructure materials, layer thicknesses and surface grating fill factors are modified, impacting light-matter interactions and consequently modifying thermal emission. We describe and validate a method for determining spectral properties of InSb under an applied direct current (DC) magnetic field, and employ this method to analyze how these properties can be tuned by modulating the field magnitude. Notably, an InSb-W metamaterial exhibiting unity narrowband emission is designed, suitable as an emitter for wavelengths around 55 μm (approximately 5.5 THz), which is magnetically tunable in bandwidth and peak wavelength.

1. Introduction

Within the fields of photonics and electromagnetism, metamaterials have received increasing attention over traditional bulk materials [1,2]. Metamaterials are specially designed photonic material structures engineered to exhibit specific thermal and optical properties that are unique from those of naturally occurring materials [3]. A typical metamaterial is composed of extremely thin material layers, often modulated with micro- or nano-scale surface patterns comparable to the wavelengths of the incoming light. These features can modify the behaviors of the inter-surface phonon polaritons (SPhPs) or surface plasmon polaritons (SPPs) within a metamaterial. Because SPhPs and SPPs greatly impact the optical resonances of dielectrics and metals, respectively, the rich microstructures of the metamaterials yield diverse radiative responses in comparison to their bulk counterparts [1,4–8].

Metamaterials can be designed to exhibit many different spectral behaviors in various regions in the electromagnetic spectra, and as such have many practical applications [3,8–32]. For example, metamaterials throughout the UV, visible, and infrared (IR) regions are employed in the areas of solar energy harvesting, biochemical sensing, communications, defense, and medical treatments [12–15,19,20]. In contrast, few metamaterial applications have materialized in the terahertz (THz) region, which covers 0.1 – 10 THz (3000 – 30 μm) [26]. However, scientists have illustrated the merit of the THz region in the areas of medical spectroscopy, security and communications [27–30]. Terahertz spectroscopy is specifically well suited for the detection of biomolecules, nucleic acids, and proteins [33] as well. Metamaterials focused on the terahertz region have also been demonstrated, presenting merit as terahertz filters and environmental sensors [34,35], efficient logical processors [36,37], and biosensor components [35].

Besides simply creating metamaterials with desirable spectral properties for a given application, researchers have also had success in dynamically tuning the spectral properties of a given metamaterial, opening the door to further applications such as self-adaptive radiative cooling and thermophotovoltaics, as well as the potential for cost reduction [38–40]. This active tuning can be induced using many techniques, including via thermal [39–41], mechanical [42–44], electrical [45,46], magnetic [47–51], or optical [52,53] means. Some dynamic tuning techniques may be suitable for certain wavelength ranges and relatively ineffective in others [38,54–56]. For example, the mechanical tuning of metamaterials has already been demonstrated in the visible [57], infrared [58] and THz [44] regions, while magnetic tuning has shown most promise in the THz region [47,59,60].

This letter involves the magnetic tunability of metamaterials in the THz region. The semiconductor material Indium Antimonide (InSb) is selected for this study due to its useful magneto-optical (MO) attributes. While many other materials, such as noble metals and ferromagnetic materials, display MO characteristics, InSb has a plasma frequency comparable to its cyclotron frequency. This allows useful optical traits, such as emissivity and transmissivity, to be modulated using magnetic fields on the order of several Tesla [61]. The doping level of semiconductors such as InSb can also be modified to adjust the plasma frequency if needed, offering further control over the field strengths needed to actively tune radiative responses [47].

As such, an analytical expression for the dielectric function of InSb is described. This expression takes into account the effect of an applied DC magnetic field, and as a result, the n and κ values of InSb are tuned when the magnetic field is present in the analysis. As InSb becomes non-reciprocal in the presence of the magnetic field, the introduction of the magnetic field also gives rise to quantum energy transport [62] and entanglement [63] phenomena, which can provide further avenues for applications of magnetically tunable optical devices. Various InSb metamaterials are theoretically and analytically demonstrated using the established dielectric functions of thin films, multilayer structures, and surface gratings. Several InSb thicknesses and grating designs are studied to understand the impact of structure geometry on selective emission. The addition of a Tungsten (W) substrate to the metamaterials is also investigated with respect to the normal emissivity of each structure, and electromagnetic fields are investigated to validate analyses and draw further conclusions.

Notably, an InSb metamaterial with unity narrowband emissivity at 55 μm (approximately 5.5 THz) has been demonstrated. Furthermore, the emissivity of this narrowband metamaterial is tuned via a magnetic field applied normal to the surface. The field modifies the peak wavelength and bandwidth of the metamaterial, and therefore allows both features to be actively tuned using an applied magnetic field. While other studies have explored magnetic tunability in the THz region with similar materials [47,48,59], this study stands out by examining the structural parameters which affect far-field resonant responses in great detail, validating analyses using EM field contours, and exemplifying a particularly useful narrowband behavior.

2. Methods

We have analytically evaluated a series of metamaterial structures consisting of InSb and W, one of which is illustrated schematically in Fig. 1(a). This grating structure is defined by a grating layer thickness of t_g, grating width w, and grating period Λ, and is built upon a W film of thickness t_2. Structures are assumed to be infinite in the x- and y-directions. An applied magnetic field with a variable strength of $0 - 6$ T is oriented perpendicular to the W film (along the z-axis).

For a generic reciprocal thermal emitter, emissivity can be expressed as $e_{\theta,\omega} = \frac{1}{2} \sum_{\mu=s,p} (1 - |\tilde{R}^{(\mu)}_{\theta,\omega}|^2 - |\tilde{T}^{(\mu)}_{\theta,\omega}|^2)$, where θ is the incident angle and ω is the angular frequency of the emitted wave. The polarization-dependent effective Fresnel reflection and transmission coefficients are given by $\tilde{R}^{(\mu)}_{\theta,\omega}$ and $\tilde{T}^{(\mu)}_{\theta,\omega}$, respectively [64]. The superscript $\mu = s$ (or p) denotes the transverse electric (or magnetic) polarization of the incident waves. The reflection and transmission coefficients
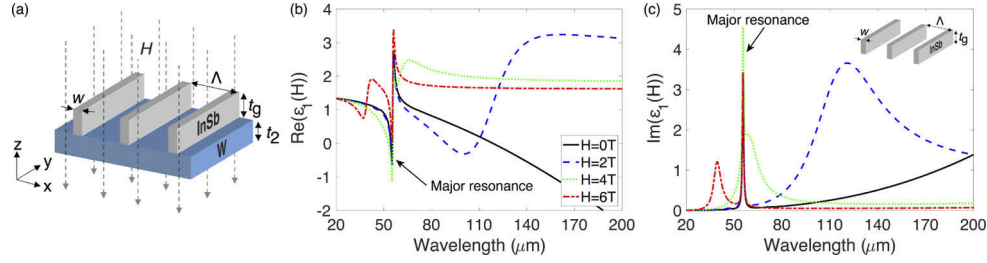
Fig. 1. (a) Schematic of InSb grating on W thin film in the presence of an applied magnetic field. (b) Real and (c) imaginary components of the magnetic field-induced refractive index $\varepsilon_1(H)$ for an InSb grating with $t_g = 7.5\mu$m, $\Lambda = 2\mu$m, and $\phi = 0.05$.

can be calculated using recursive Fresnel relations at each interface [65]. For nonreciprocal emitters which have anisotropic permittivity tensors, such as those incorporating magneto-optical materials, Kirchhoff's Law is violated [66–69], and the absorptivity $\alpha_{\theta,\omega}$ cannot be assumed to be equal to the emissivity. In this case, the aforementioned emissivity equation is only valid for cases of normal incidence ($\theta = 0°$). For this reason, this work focuses on normal emissivities of the selected metamaterials.

The normal z-component of the wave vector for medium i is given by $k_{i,z} = \sqrt{\omega^2\varepsilon_i(\omega)/c^2 - k_\rho^2}$, where $\varepsilon_i(\omega)$ is the relative permittivity of medium i as a function of angular frequency ω, k_ρ is the magnitude of the in-plane wave vector ($k_\rho = 0$ for normal incidence), and c is the speed of light in vacuum [65]. The dielectric function is related to the real (n) and imaginary (κ) parts of the refractive index as $\sqrt{\varepsilon} = n + j\kappa$, where j is the imaginary unit [64]. The dielectric functions for the grating layers are determined using the second order effective medium theory (EMT), which is used within a Rigorous Coupled Wave Analysis (RCWA) model [70–72]. Other studies have also validated the use of the EMT with anisotropic magneto-optical materials, noting agreement with respect to both alternative numerical models and experimental data [73–76]. To provide further validation and expand the applicability of the EMT, spectra are calculated using both the EMT and RCWA methods and compared within this work, where strong agreement is noted for nearly all cases. The RCWA package used to calculate spectra is also used to produce electromagnetic (EM) field contour plots [70–72].

Using the EMT method, the effective transverse electric and transverse magnetic dielectric functions of the grating layers are given by [64]

$$\varepsilon_{TE,2} = \varepsilon_{TE,0}\left[1 + \frac{\pi^2}{3}\left(\frac{\Lambda}{\lambda}\right)^2 \phi^2(1-\phi)^2 \frac{(\varepsilon_A - \varepsilon_B)^2}{\varepsilon_{TE,0}}\right] \tag{1}$$

and

$$\varepsilon_{TM,2} = \varepsilon_{TM,0}\left[1 + \frac{\pi^2}{3}\left(\frac{\Lambda}{\lambda}\right)^2 \phi^2(1-\phi)^2(\varepsilon_A - \varepsilon_B)^2\varepsilon_{TE,0}\left(\frac{\varepsilon_{TM,0}}{\varepsilon_A\varepsilon_B}\right)^2\right], \tag{2}$$

respectively, where Λ is the grating period, λ is the incident wavelength, and ϕ is the filling ratio of the grating defined as w/Λ. The relative permittivities of the two materials in the surface grating, InSb and air, are ε_A and ε_B, respectively (with $\varepsilon_B = 1$). $\varepsilon_{TE,0}$ and $\varepsilon_{TM,0}$ are the zeroth order transverse electric and transverse magnetic effective dielectric functions, which are given by $\varepsilon_{TE,0} = \phi\varepsilon_A + (1-\phi)\varepsilon_B$ and $\varepsilon_{TM,0} = (\phi/\varepsilon_A + (1-\phi)/\varepsilon_B)^{-1}$, respectively [64].

In this work, the dielectric function of W is determined based on n and κ values from the literature [77]. In the absence of a magnetic field, the dielectric function for InSb is given by [78]

$$\varepsilon = \varepsilon_\infty\left(1 + \frac{\omega_L^2 - \omega_T^2}{\omega_T^2 - \omega^2 - j\Gamma\omega} - \frac{\omega_p^2}{\omega(\omega + j\gamma)}\right) \tag{3}$$

where ε_∞ is the high-frequency dielectric constant, ω_L is the longitudinal optical phonon frequency, ω_T is the transverse optical phonon frequency, Γ is the phonon damping constant, and γ is the free-carrier damping constant. The plasma frequency ω_p of free carriers of density N and effective mass m^* is described by $\omega_p = N q_e^2 / m^* \varepsilon_0 \varepsilon_\infty$, where q_e and ε_0 are the elementary charge and vacuum permittivity, respectively, and values for the InSb-specific constants are taken from the literature [47,48].

Under a magnetic field H applied along the z-direction, the permittivity tensor of InSb takes the following form [47,48]:

$$\hat{\varepsilon}(H) = \begin{pmatrix} \varepsilon_1(H) & -j\varepsilon_2(H) & 0 \\ j\varepsilon_2(H) & \varepsilon_1(H) & 0 \\ 0 & 0 & \varepsilon_3 \end{pmatrix} \tag{4}$$

where

$$\varepsilon_1(H) = \varepsilon_\infty \left(1 + \frac{\omega_L^2 - \omega_T^2}{\omega_T^2 - \omega^2 - j\Gamma\omega} + \frac{\omega_p^2(\omega + j\gamma)}{\omega[\omega_c - (\omega + j\gamma)^2]} \right), \tag{5a}$$

$$\varepsilon_2(H) = \frac{\varepsilon_\infty \omega_p^2 \omega_c}{\omega[(\omega + j\gamma)^2 - \omega_c^2]}, \tag{5b}$$

$$\varepsilon_3 = \varepsilon_\infty \left(1 + \frac{\omega_L^2 - \omega_T^2}{\omega_T^2 - \omega^2 - j\Gamma\omega} - \frac{\omega_p^2}{\omega(\omega + j\gamma)} \right). \tag{5c}$$

The magnetic field contributes to the permittivity components $\varepsilon_1(H)$ and $\varepsilon_2(H)$ via the the cyclotron frequency term, which is given by $\omega_c = q_e H / m^*$. For the analyses herein, $q_e = 1.602 \times 10^{-19}$ C, and $m^* = 2.004 \times 10^{-32}$ kg. Using this method, we have calculated the wavelength-dependent n and κ values of $\varepsilon_1(H)$ for an InSb grating structure ($t_g = 7.5\mu m$, $\Lambda = 2\mu m$, and $\phi = 0.05$) subjected to various magnetic field strengths, as shown in Fig. 1(b) and Fig. 1(c), respectively. It can be seen that the magnetic field has a dramatic effect on these optical functions.

With the anisotropy of the permittivity tensor as expressed in Eq. (4), the equation for the normal z-component of the wave vector can be re-written as $k_{o,z}(H) = \sqrt{\omega^2 \varepsilon_1(H)/c^2 - k_\rho^2}$ for ordinary waves and $k_{e,z}(H) = \sqrt{\omega^2 \varepsilon_1(H)/c^2 - k_\rho^2 \varepsilon_1(H)/\varepsilon_3}$ for extraordinary waves [47]. For a case of normal incidence, $k_\rho = 0$, leaving only $\varepsilon_1(H)$ to contribute to this dispersion relation. While this technique limits the study of other incidence angles, it offers a useful alternative that is far less computationally expensive and simplified, permitting increased availability to researchers interested in exploring magneto-optical materials.

In addition, for optical systems which consider magnetized media, the magneto-optical Kerr effect (MOKE) may induce a modification in the polarization state of reflected light. This effect is brought on by the presence of off-diagonal components in the permittivity tensor. For the perpendicular magnetic field orientation considered within this work - a polar Kerr configuration - the tensor components $j\varepsilon_2(H)$ and $-j\varepsilon_2(H)$ are the main contributors to the MOKE [61,79]. However, for this specific case of magnetized InSb within Tesla-scale magnetic fields, previous works have verified that the thermal emission of comparable InSb-based metamaterials in the terahertz region is unaffected by the polarization conversion [47,48].

Combining these assumptions with the aforementioned equations, we have calculated the normal emissivity for a variety of metamaterials incorporating InSb as both a grating layer and a thin film layer under an applied magnetic field.

3.   Results and discussion

In the absence of the magnetic field, the TE and TM emissivities as functions of wavelength are shown in Figs. 2(a) and 2(c) for selected InSb thin film and grating designs. An emission spike is present around 55 μm, which aligns with the major resonant wavelengths of n and κ in the zero-field case shown in Figs. 1(b) and 1(c). The emissivity is observed to scale with thickness. These trends are consistent for both TE and TM polarizations, though the TM emissivities are slightly lesser in magnitude for the grating structures. However, neither changes in thickness nor the geometric features of the grating modify the SPhP resonances of the InSb structures in these cases. The pure InSb structures have obvious resonances in the $20 - 100$ μm wavelength region, yet their potential application as an emitter is hampered by relatively low emissivities and a lack of focus on a specific wavelength.
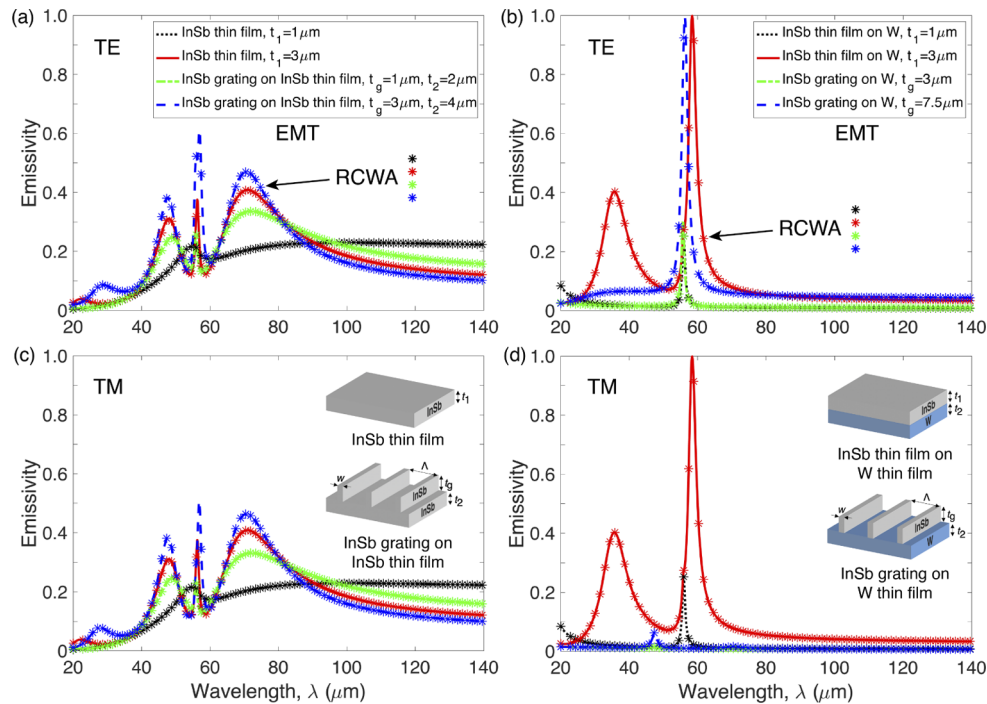
Fig. 2. TE (a) and TM (c) emissivities of InSb thin film and grating structures; TE (b) and TM (d) emissivities of InSb-W thin film and grating structures. All gratings have $\Lambda = 2\mu m$ and $\phi = 0.05$. For (b) and (d), $t_2 = 10$ μm. EMT results are plotted using various lines, and associated RCWA results are plotted using markers, showing agreement between the two methods.

In contrast to the pure InSb metamaterials, we calculate the emissivities of InSb thin film and grating layers atop W base layers in Fig. 2(b). The W base suppresses many of the smaller oscillations before and after the prominent 55 μm peak for the thin film cases, which we attribute to the introduction of SPPs from the W layer. The light-matter interactions are further modified when the InSb-W grating structures are introduced, as shown in Fig. 2(b). The chosen geometric factors suppress the pre-peak resonances, leaving only a pronounced narrowband at the major InSb resonance wavelength. While the thin film emissivities are again identical between the TE and TM cases, the InSb-W grating structures suppress the TM emissivity in favor of the TE emissivity. With a grating thickness of $t_g = 7.5$ μm, the unity narrowband TE emission of the InSb-W grating structure represents an exemplary design for a THz emitter around 55 μm.

The effects of different structural parameters on emissivity via SPhPs and SPPs are supported by the EM field contours displayed in Fig. 3. Enhanced absorption at specific frequencies can be attributed to the excitation of EM field resonances [71,72]. By comparing the EM fields of different structures at the same resonance frequencies, the spectra results can be validated, and geometric and material factors crucial to the radiative properties can be identified.
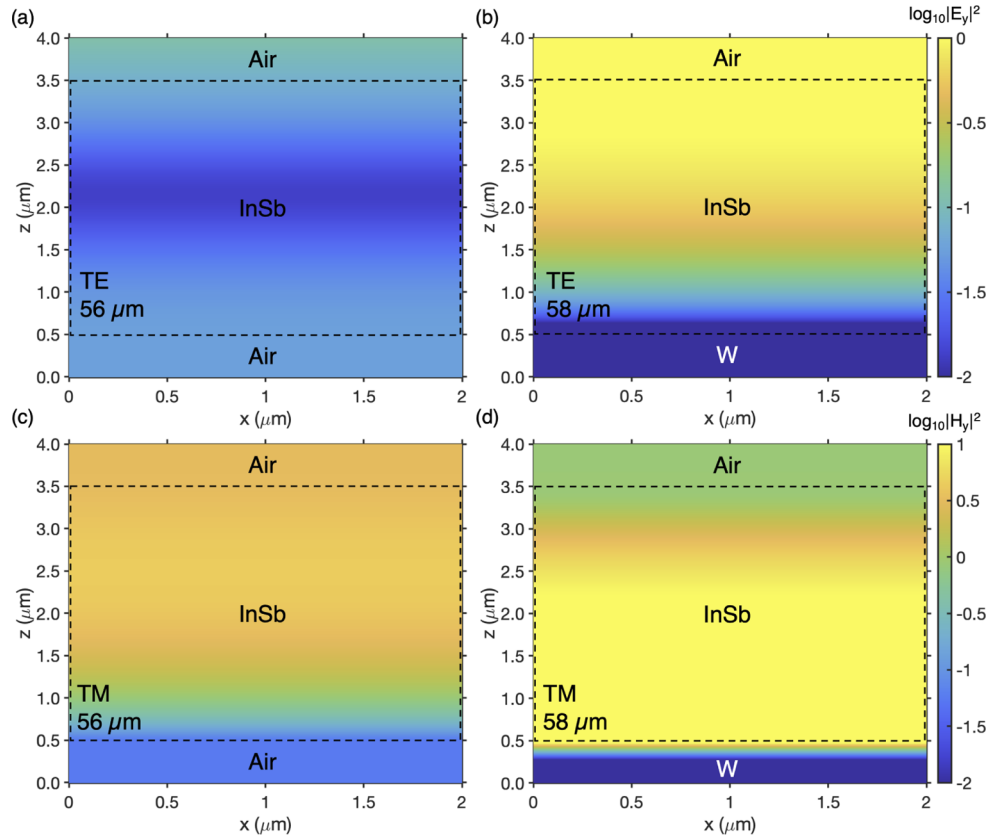

Fig. 3. Square of field magnitude for 3 μm InSb thin films with and without a 10 μm W substrate. (a) TE and (c) TM field contours for InSb thin film. (b) TE and (d) TM field contours for InSb thin film with W substrate. Fields are evaluated at their strongest resonant frequency to illustrate the effect of the W substrate.

In Fig. 3, EM field differences are presented for 3 μm InSb thin films, both with and without a W substrate. Their fields are evaluated at slightly different wavelengths to accommodate the strongest resonance frequency of each structure. For both TE and TM waves, both structures with the W substrate show much stronger field strengths, most notably within their InSb layers. When the W is added, the InSb layer experiences field strengths approximately one order of magnitude larger in the TE case, and one-half order of magnitude larger in the TM case. This illustrates that the introduction of SPPs from the W layer help amplify the existing InSb major resonance that exists near wavelengths of 55 μm.

The analyses in Fig. 4 further detail the effects of grating parameters t_g, Λ and ϕ on the normal emissivities of the InSb-W metamaterial. For larger values of t_g in Fig. 4(a), the InSb thickness increases the surface resonance wavelengths, as well as the TE emissivity in most cases. When t_g is scaled past a certain threshold (7.5 μm in this case), the resonance specific to the t_g alterations moves past the major InSb resonance, the latter of which is still apparent. This indicates that

the resonances corresponding to modifications in t_g and the original zero-field InSb resonance identified in Figs. 1(b) and 1(c) are not entirely interdependent and can be aligned to achieve strong emitter performance. In contrast, the TM resonant wavelengths are unmodified by changes in grating thickness, while the magnitude of the emissivity is strongly correlated with grating thickness, as displayed in Fig. 4(d).
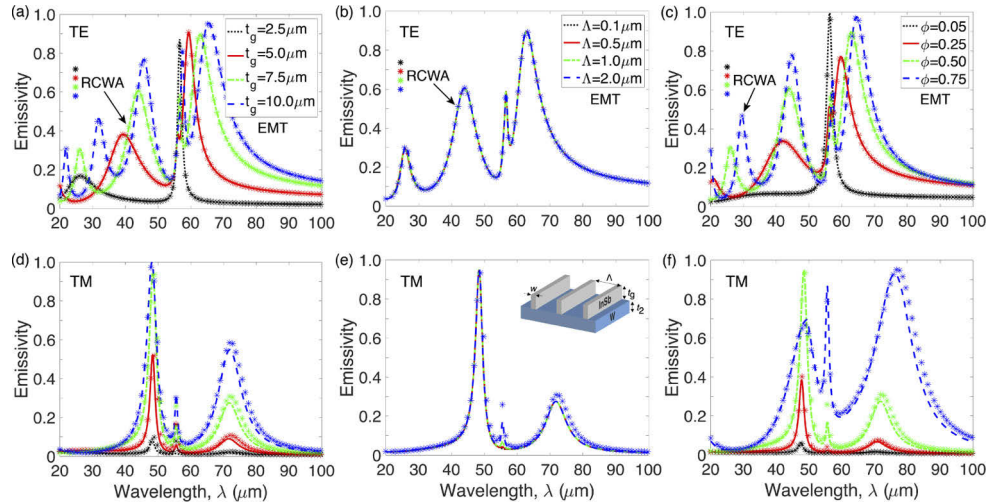

Fig. 4. (a) TE and (d) TM emissivities of InSb-W grating structures of varying grating thickness t_g, with $\Lambda = 2$ μm and $\phi = 0.5$. (b) TE and (e) TM emissivities of InSb-W grating structures of varying grating period Λ, with $t_g = 7.5$ μm and $\phi = 0.5$. (c) TE and (f) TM emissivities of InSb-W grating structures of varying grating fill factor ϕ, with $t_g = 7.5$ μm and $\Lambda = 2$ μm. For all cases, $t_2 = 10$ μm. EMT results are plotted using various lines, and associated RCWA results are plotted using markers, showing agreement between the two methods.

The emissivity of this metamaterial has a very weak dependence on the grating period Λ, as displayed in Figs. 4(b) and 4(e). Modifying the period does not change the grating thickness, though it does alter the amount of InSb in a given unit area. Therefore, the fact that there is an extremely minor effect aligns with previous analyses as well as Eqs. (1) and (2). For this reason, metamaterial design with InSb gratings can be performed with a large variety of periods without significant changes in performance, expanding the potential accessibility of this metamaterial. It should also be noted that only grating periods significantly smaller than the wavelengths of interest are considered here, in order to conform to the restrictions of the effective medium theory. It is possible that significantly larger grating periods may induce larger changes in the emissivity than those seen in Figs. 4(b) and 4(e).

Based on Eqs. (1) and (2), the relative permittivity of a grating is heavily dependent upon the fill factor ϕ. This is exemplified in Figs. 4(c) and 4(f), where both resonant wavelength and emissivity are tuned by varying the fill factor. As the fill factor increases, the amount of InSb in the grating increases, while the amount of air in the grating is reduced. Hence, the gratings with reduced fill factors exhibit less apparent minor InSb resonances, although the major zero-field InSb resonance remains prominent. These effects are consistent between the TE and TM cases, although some TE and TM resonances do manifest at different wavelengths. This technique is applied to design the metamaterial exhibiting permanent narrowband TE emissivity in Fig. 4(c) ($\phi = 0.05$), which has great potential for an InSb-based THz emitter. Though the small fill factor of this design does hamper the TM emissivity, it maximizes the focus of the emitter on one specific wavelength which enhances its usefulness and tunability. Larger fill factors may

be useful for geometrically tuning peak location since the largest peak emissivity is not greatly reduced, but this approach adds many minor emissivity peaks which would reduce the efficiency of such an emitter.

The field contours of Figs. 5 and 6 further illustrate that grating parameters play a significant role in the magnitude and location of many emissivity resonances. Firstly, thicker gratings are observed to enhance off-peak resonances in both TE and TM cases, notably at wavelengths of 44 and 72 μm, respectively. This is corroborated by the field contours of Fig. 5, where gratings 7.5 μm thick show far higher field magnitudes when compared with gratings 2.5 μm thick.
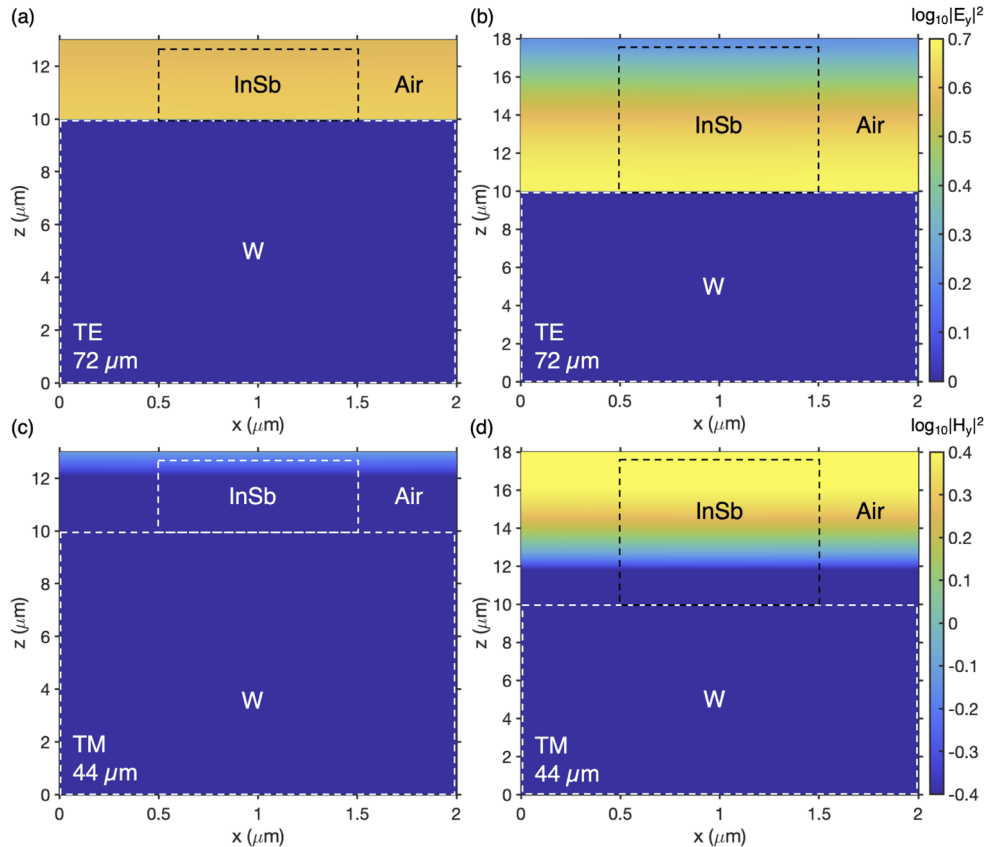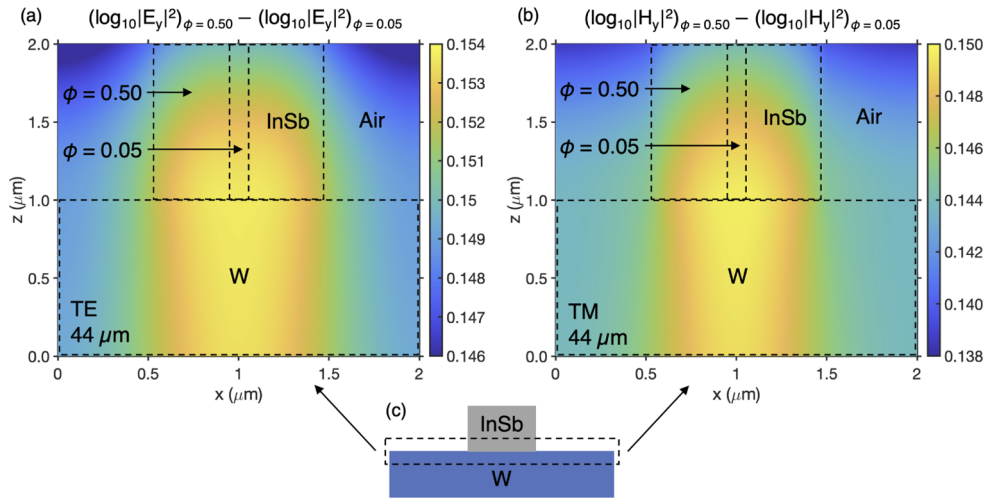

Fig. 5. Square of field magnitude for InSb grating structures of varying t_g on 10 μm W substrates. TE field contours at 72 μm with (a) $t_g = 2.5$ μm and (b) $t_g = 7.5$ μm. TM field contours at 44 μm with (c) $t_g = 2.5$ μm and (d) $t_g = 7.5$ μm. The fill factor ϕ is equal to 0.50 for all cases.

Additionally, Fig. 6 depicts how the fill factor has a similar effect on the EM field. The difference in field magnitude for fill factors of $\phi = 0.50$ and $\phi = 0.05$ is shown for a wavelength of 44 μm, revealing a pronounced effect specifically at the InSb-W interface. The larger grating produces stronger resonances both within the structure itself, as well as within the cavities between the gratings. This justifies the enhanced emissivity at off-peak wavelengths.

The analyses in these figures suggest that the chosen InSb-W structure is heavily impacted by resonances occurring within the InSb, which are significantly amplified by the W substrate. In all cases, field activity at non-major peak wavelengths is enhanced within the InSb when the amount of this material increases. This leads to emissivity enhancements at these wavelengths, as seen in the various spectra results. In addition, cavity resonances play an important role. Increasing

Fig. 6. Difference in square of field magnitude between InSb grating structures of $\phi = 0.50$ and $\phi = 0.05$. (a) Difference in TE field contours at 44 μm. (b) Difference in TM field contours at 44 μm. Grating thickness t_g is equal to 7.5 μm, and the W substrate is 10 μm for both cases. (c) Schematic depicting the section of structure at the InSb-W interface that is analyzed.

either the grating thickness or the grating fill factor will lead to more pronounced cavities in the structure. Furthermore, both a larger grating thickness and a larger fill factor lead to very similar emissivity resonances in Fig. 4, which are comparable in both location and magnitude. The EM field contours also reveal increased activity within these cavity regions when these geometric parameters are increased (though they are secondary in strength to the enhancements within the materials themselves). Altogether, this indicates that these additional resonant modes are attributable to both the properties of InSb and the intensity of cavities within the structure. Fine-tuning the relative amount of this material and the cavity geometries can eliminate the non-major resonant modes, leaving a useful narrowband behavior near 55 μm.

Finally, we have studied the dramatic effect of the magnetic field on the narrowband emissivity of an InSb-W grating structure. Figure 7 shows the normal emissivity of a grating structure with $t_g = 7.5 \ \mu m$, $\Lambda = 2 \ \mu m$, and $\phi = 0.05$ under applied fields of 0, 4, 5 and 6 T. The plotted curves represent the data obtained from the EMT implementation, while the corresponding square markers show the near-identical results from the RCWA approach. In Fig. 7(a), Tesla-scale magnetic fields significantly modify the TE light-matter interactions by widely broadening the resonant wavelengths over a range of 25 μm, while still maintaining the near-unity emissivity resonance peak. The emissivity initially red-shifts at lower magnetic field values, before being blue-shifted when the field intensity increases. The small value of fill factor ϕ was chosen to maximize the tunability of the structure, as discussed previously. While this results in minimal TM contributions (Fig. 7(b)), there is still an obvious shift in the TM resonance wavelengths in response to the induced magnetic field. This indicates that an external magnetic field can be applied to tune both the TE and TM emissivities of this metamaterial - consistent with the theory presented in Section 2. As noted earlier, the applied magnetic field affects only the cyclotron frequency term ω_c in Eq. (5a), which enables it to modify the emissivity of the metamaterial. The peak shift at these field values in both the TE and TM cases is attributed to the cyclotron resonance line carrying the free-carrier dispersion to different frequencies, which occurs when ω_c becomes comparable to ω_T[78].
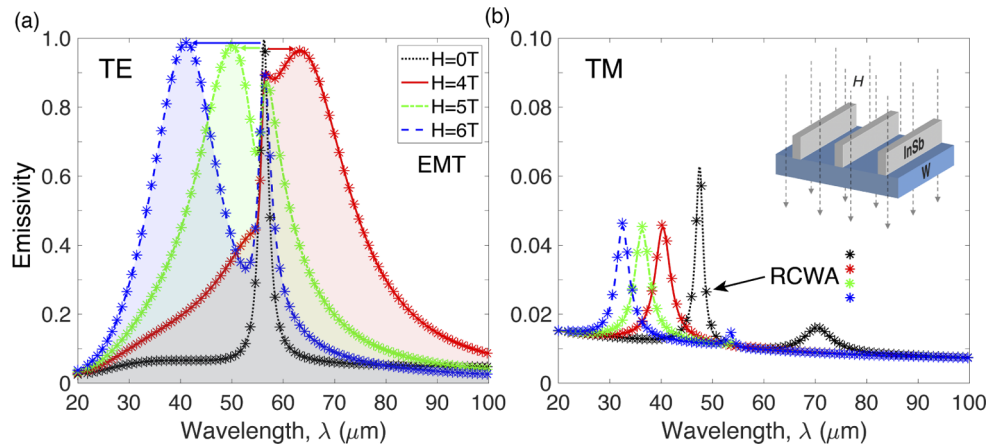
Fig. 7. (a) TE and (b) TM emissivities of InSb-W grating structure, with $t_g = 7.5 \ \mu m$, $\Lambda = 2$ μm, $\phi = 0.05$ and $t_2 = 10 \ \mu m$ under external magnetic fields of varying magnitudes. Field-induced curves in (a) are color-filled to highlight the broadband red or blue emissivity shifts brought on by the magnetic field. Arrows denote the direction of the dominant resonance shift from the original narrowband peak to longer (red) or shorter (blue) wavelengths. EMT results are plotted using various lines, and associated RCWA results are plotted using markers, showing agreement between the two methods.

For this InSb-W metamaterial, the applied magnetic field broadens the bandwidth and shifts the resonant wavelength of the emissivity. At large values of H, the magnetic field modifies the values of $\varepsilon_1(H)$ in Eq. (5a) such that the extraordinary wave dispersion becomes hyperbolic [47]. This effect generates new broadband modes similar to those of SPPs which can be tuned by modifying the magnitude of H, but does not affect the original major InSb narrowband resonance – results which are consistent with previous studies [47,78]. These behaviors open additional avenues for manipulating the optical emission properties of metamaterials, as well as remotely sensing magnetic fields in hard-to-reach spaces, such as inside high-energy particle detectors or electrical power systems. Additionally, the 55 μm peak location corresponds to a thermal emitter of roughly 50 K [80], suggesting a suitable application as a sensor for materials at cryogenic temperatures and deep-space objects, as these objects would emit radiation near the strongest resonance peaks of this metamaterial.

4. Conclusion

In summary, we have investigated the optical emissive properties of InSb-based metamaterial structures, both with and without a W substrate, under the influence of a variety of geometric factors. Electromagnetic contour plots validate these analyses and provide a more detailed explanation of the observed behaviors. We have also examined the same properties of InSb-W metamaterials under an applied magnetic field.

A method for analytically expressing the dielectric function of InSb has been combined with the effective medium theory to enable this study. The EMT results are also validated with respect to a pure RCWA approach, postulating that the EMT is valid for this magneto-optical system, thus further expanding its applicability. In the absence of the magnetic field, the volume fraction of the top InSb layer of the structure has the most prominent effect on the tunable normal emissivity. The inclusion of a W substrate suppresses many of the minor peaks while amplifying the most prominent resonance. This enhancement of the emissivity at a specific wavelength could be taken advantage of in many photonic applications. We attribute these behaviors to changes in surface

polariton resonances arising from metamaterial structural variations. We demonstrate that an applied magnetic field has the capability to tune the emissivity of an InSb-W grating structure, which has demonstrated unity narrowband emissivity around 55 μm in a zero field case. Through its effect on the cyclotron resonances, the external field is highly effective in red- and blue-shifting the peak TE emissivity wavelength and widening the narrowband to a broadband, while still preserving its near-unity magnitude. These findings may benefit applications in the THz region, as well as magnetic sensing in electrical systems, non-destructive sensing and imaging [29], pharmaceuticals [81], cryogenic sensing and astronomical observation [27,82].

Disclosures. The authors declare no conflicts of interest.

Data availability. Data underlying the results presented in this paper are not publicly available at this time but may be obtained from the authors upon reasonable request.

References

1. D. Lin, P. Fan, E. Hasman, and M. L. Brongersma, "Dielectric gradient metasurface optical elements," Science **345**(6194), 298–302 (2014).
2. C. M. Soukoulis and M. Wegener, "Optical metamaterials - more bulky and less lossy," Science **330**(6011), 1633–1634 (2010).
3. A. V. Kildishev, A. Boltasseva, and V. M. Shalaev, "Planar photonics with metasurfaces," Science **339**(6125), 1232009 (2013).
4. R. Hillenbrand, T. Taubner, and F. Keilmann, "Phonon-enhanced light-matter interaction at the nanometre scale," Nature **418**(6894), 159–162 (2002).
5. A. Huber, N. Ocelic, D. Kazantsev, and R. Hillenbrand, "Near-field imaging of mid-infrared surface phonon polariton propagation," Appl. Phys. Lett. **87**(8), 081103 (2005).
6. W. L. Barnes, A. Dereux, and T. W. Ebbesen, "Surface plasmon subwavelength optics," Nature **424**(6950), 824–830 (2003).
7. J. D. Caldwell, L. Lindsay, V. Giannini, I. Vurgaftman, T. L. Reinecke, S. A. Maier, and O. J. Glembocki, "Low-loss, infrared and terahertz nanophotonics using surface phonon polaritons," Nanophotonics **4**(1), 44–68 (2015).
8. J. B. Pendry, D. Schurig, and D. R. Smith, "Controlling electromagnetic fields," Science **312**(5781), 1780–1782 (2006).
9. G. Oliveri, D. H. Werner, and A. Massa, "Reconfigurable electromagnetics through metamaterials - a review," Proc. IEEE **103**(7), 1034–1056 (2015).
10. C. L. Holloway, E. F. Kuester, J. O. J. A. Gordon, J. Booth, and D. R. Smith, "An overview of the theory and applications of metasurfaces: The two-dimensional equivalents of metamaterials," IEEE Antennas Propag. Mag. **54**(2), 10–35 (2012).
11. S. Sarkar, R. O. Behunin, and J. G. Gibbs, "Shape-dependent, chiro-optical response of uv-active, nanohelix metamaterials," Nano Lett. **19**(11), 8089–8096 (2019).
12. K. Liu, S. Jiang, D. Ji, X. Zeng, N. Zhang, H. Song, Y. Xu, and Q. Gan, "Super absorbing ultraviolet metasurface," IEEE Photonics Technol. Lett. **27**(14), 1539–1542 (2015).
13. M. A. Baqir and P. K. Choudhury, "Hyperbolic metamaterial-based uv absorber," IEEE Photonics Technol. Lett. **29**(18), 1548–1551 (2017).
14. F. Dincer, O. Akgol, M. Karaaslan, E. Unal, and C. Sabah, "Polarization angle independent perfect metamaterial absorbers for solar cell applications in the microwave, infrared, and visible regime," Prog. Electromagn. Res. **144**, 93–101 (2014).
15. P. Rufangura and C. Sabah, "Wide-band polarization independent perfect metamaterial absorber based on concentric rings topology for solar cells application," J. Alloys Compd. **680**, 473–479 (2016).
16. W. Cai, U. K. Chettiar, A. V. Kildishev, and V. M. Shalaev, "Optical cloaking with metamaterials," Nat. Photonics **1**(4), 224–227 (2007).
17. N. Liu, H. Guo, L. Fu, S. Kaiser, H. Schweizer, and H. Giessen, "Three-dimensional photonic metamaterials at optical frequencies," Nat. Mater. **7**(1), 31–37 (2008).
18. E. M. Carapezza, ed., *Proceedings of SPIE*, vol. 9456 (SPIE, Baltimore, Maryland, United States, 2015).
19. H. Wang, V. P. Sivan, A. Mitchell, G. Rosengarten, and P. Phelan, "Highly efficient selective metamaterial absorber for high-temperature solar thermal energy harvesting," Sol. Energy Mater. Sol. Cells **137**, 235–242 (2015).
20. K. D. Desmet, D. A. Paz, J. J. Corry, J. T. Eells, M. T. T. Wong-Riley, M. M. Henry, E. V. Buchmann, M. P. Connelly, J. V. Dovi, H. L. Liang, D. S. Henshel, R. L. Yeager, D. S. Millsap, J. Lim, L. J. Gould, R. Das, M. Jett, B. D. Hodgson, D. Margolis, and H. T. Whelan, "Clinical and experimental applications of nir-led photobiomodulation," Photomed. Laser Surg. **24**(2), 121–128 (2006).

21. G. Bellisola and C. Sorio, "Infrared spectroscopy and microscopy in cancer research and diagnosis," Am. J. Cancer Res. **2**(1), 1–21 (2012).

22. J. A. Montoya, Z. Tian, S. Krishna, and W. J. Padilla, "Ultra-thin infrared metamaterial detector for multicolor imaging applications," Opt. Express **25**(19), 23343–23355 (2017).

23. S. Ogawa, K. Okada, N. Fukushima, and M. Kimata, "Wavelength selective uncooled infrared sensor by plasmonics," Appl. Phys. Lett. **100**(2), 021111 (2012).

24. R. Xu and Y. Lin, "Tunable infrared metamaterial emitter for gas sensing application," Nanomaterials **10**(8), 1442 (2020).

25. N. Liu, M. Mesch, T. Weiss, M. Hentschel, and H. Giessen, "Infrared perfect absorber and its application as plasmonic sensor," Nano Lett. **10**(7), 2342–2348 (2010).

26. W. Xu, L. Xie, and Y. Ying, "Mechanisms and applications of terahertz metamaterial sensing: a review," Nanoscale **9**(37), 13864–13878 (2017).

27. M. Tonouchi, "Cutting-edge terahertz technology," Nat. Photonics **1**(2), 97–105 (2007).

28. J. Son, S. J. Oh, and H. Cheon, "Potential clinical applications of terahertz radiation," J. Appl. Phys. **125**(19), 190901 (2019).

29. S. Galoda and G. Signh, "Fighting terrorism with terahertz," IEEE Potentials **26**(6), 24–29 (2007).

30. S. Zhong, "Progress in terahertz nondestructive testing: A review," Front. Mech. Eng. **14**(3), 273–281 (2019).

31. A. Ghanekar, J. Ji, and Y. Zheng, "High-rectification near-field thermal diode using phase change period nanostructure," Appl. Phys. Lett. **109**(12), 123106 (2016).

32. A. Ghanekar, M. Ricci, Y. Tian, O. Gregory, and Y. Zheng, "Strain-induced modulation of near-field radiative transfer," Appl. Phys. Lett. **112**(24), 241104 (2018).

33. H. Ou, F. Lu, Z. Xu, and Y. Lin, "Terahertz metamaterial with multiple resonances for biosensing application," Nanomaterials **10**(6), 1038 (2020).

34. P. Liu, Z. Liang, Z. Lin, Z. Xu, R. Xu, D. Yao, and Y. Lin, "Actively tunable terahertz chain-link metamaterial with bidirectional polarization-dependent characteristic," Sci. Rep. **9**(1), 9917 (2019).

35. Y. Liu, C. Fang, G. Han, Y. Shao, Y. Huang, H. Wang, Y. Wang, C. Zhang, and Y. Hao, "Ultrathin corrugated metallic strips for ultrawideband surface wave trapping at terahertz frequencies," IEEE Photonics J. **9**(1), 1–8 (2017).

36. Z. Xu, Z. Lin, S. Cheng, and Y. Lin, "Reconfigurable and tunable terahertz wrenchshape metamaterial performing programmable characteristic," Opt. Lett. **44**(16), 3944–3947 (2019).

37. Z. Xu and Y. Lin, "A stretchable terahertz parabolic-shaped metamaterial," Adv. Opt. Mater. **7**(19), 1900379 (2019).

38. J. P. Turpin, J. A. Bossard, K. L. Morgan, D. H. Werner, and P. L. Werner, "Reconfigurable and tunable metamaterials: A review of the theory and applications," Int. J. Antennas and Propagation **2014**, 1–18 (2014).

39. T. Cao, X. Zhang, W. Dong, L. Lu, X. Zhou, X. Zhuang, J. Deng, X. Cheng, G. Li, and R. E. Simpson, "Tuneable thermal emission using chalcogenide metasurface," Adv. Opt. Mater. **6**(16), 1800169 (2018).

40. Y. Qu, Q. Li, K. Du, L. Cai, J. Lu, and M. Qiu, "Dynamic thermal emission control based on ultrathin plasmonic metamaterials including phase-changing material gst," Laser Photonics Rev. **11**(5), 1700091 (2017).

41. T. H. Nguyen, S. T. Biu, X. C. Nguyen, D. L. Vu, and X. K. Bui, "Tunable broadband-negative-permeability metamaterials by hybridization at thz frequencies," RSC Adv. **10**(47), 28343–28350 (2020).

42. R. Xu, J. Luo, J. Sha, J. Zhong, Z. Xu, Y. Tong, and Y. Lin, "Stretchable ir metamaterial with ultra-narrowband perfect absorption," Appl. Phys. Lett. **113**(10), 101907 (2018).

43. Z. Wang, P. Lv, M. Becton, J. Hong, L. Zhang, and X. Chen, "Mechanically tunable near-field radiative heat transfer between monolayer black phosphorus sheets," Langmuir **36**(40), 12038–12044 (2020).

44. X. Su, C. Feng, Y. Zeng, and H. Yu, "A dual-band tunable metamaterial absorber based on pneumatic actuation mechanism," Opt. Commun. **459**, 124885 (2020).

45. F. Chen, Y. Cheng, and H. Luo, "A broadband tunable terahertz metamaterial absorber based on single-layer complementary gammadion-shaped graphene," Materials **13**(4), 860 (2020).

46. Y. Qi, Y. Zhang, C. Liu, T. Zhang, B. Zhang, L. Wang, X. Deng, X. Wang, and Y. Yu, "A tunable terahertz metamaterial absorber composed of hourglass-shaped graphene arrays," Nanomaterials **10**(3), 533 (2020).

47. E. Moncada-Villa, V. Fernanandez-Hurtado, F. J. Garcia-Vidal, A. Garcia-Martin, and J. C. Cuevas, "Magnetic field control of near-field radiative heat transfer and the realization of highly tunable hyperbolic thermal emitters," Phys. Rev. B **92**(12), 125418 (2015).

48. E. Moncada-Villa and J. C. Cuevas, "Near-field radiative heat transfer between one-dimensional magnetophotonic crystals," Phys. Rev. B **103**(7), 075432 (2021).

49. B. Hu, Y. Zhang, and Q. J. Wang, "Surface magneto plasmons and their applications in the infrared frequencies," Nanomaterials **4**(4), 383–396 (2015).

50. V. I. Pipa, A. I. Liptunga, and V. Morozhenko, "Thermal emission of one-dimensional magnetophotonic crystals," J. Opt. **15**(7), 075104 (2013).

51. H. Wang, H. Wu, and Z. Shen, "Nonreciprocal optical properties of thermal radiation with sic grating magneto-optical materials," Opt. Express **25**(16), 19609–19618 (2017).

52. C. Lee, H. J. Choi, and H. Jeong, "Tunable metasurfaces for visible and swir applications," Nano Convergence **7**(1), 3 (2020).

53. M. J. Dicken, K. Aydin, I. M. Pryce, L. A. Sweatlock, E. M. Boyd, J. M. S. Walavalkar, and H. A. Atwater, "Frequency tunable near-infrared metamaterials based on vo2 phase transition," Opt. Express **17**(20), 18330–18339 (2009).

54. Y. Li, Y. Shen, S. Cao, X. Zhang, and Y. Meng, "Thermally triggered tunable vibration mitigation in hoberman spherical lattice metamaterials," Appl. Phys. Lett. **114**(19), 191904 (2019).

55. X. Jia, X. Wang, C. Yuan, Q. Meng, and Z. Zhou, "Novel dynamic tuning of broadband visible metamaterial perfect absorber using graphene," Appl. Phys. Lett. **120**(3), 033101 (2016).

56. T. Driscoll, S. Palit, M. M. Qazilbash, M. Brehm, F. Keilmann, B. Chae, S. Yun, H. Kim, S. Y. Cho, N. M. Jokerst, D. R. Smith, and D. N. Basov, "Dynamic tuning of an infrared hybrid-metamaterial resonance using vanadium dioxide," Appl. Phys. Lett. **93**(2), 024101 (2008).

57. P. Gutruf, C. Zou, W. Withayachumnankul, M. Bhaskaran, S. Sriram, and C. Fumeaux, "Mechanically tunable dielectric resonator metasurfaces at visible frequencies," ACS Nano **10**(1), 133–141 (2016).

58. X. Liu, Y. Tian, F. Chen, A. Ghanekar, M. Antezza, and Y. Zheng, "Continuously variable emission for mechanical deformation induced radiative cooling," Commun. Mater. **1**(1), 95 (2020).

59. G. Sharma, A. Lakhtakia, S. Bhattacharyya, and P. K. Jain, "Magnetically tunable metasurface comprising inas and insb pixels for absorbing terahertz radiation," Appl. Opt. **59**(31), 9673–9680 (2020).

60. K. Li, X. Ma, Z. Zhang, L. Wang, H. Hu, Y. Xu, and G. Song, "Highly tunable terahertz filter with magneto-optical bragg grating formed in semiconductor-insulator-semiconductor waveguides," AIP Adv. **3**(6), 062130 (2013).

61. G. Armelles, A. Cebollada, A. Garcia-Martin, and M. U. Gonzalez, "Magnetoplasmonics: Combining magnetic and plasmonic functionalities," Adv. Opt. Mater. **1**(1), 10–35 (2013).

62. P. Doyeux, S. A. H. Gangaraj, G. W. Hanson, and M. Antezza, "Giant interatomic energy-transport amplification with nonreciprocal photonic topological insulators," Phys. Rev. Lett. **119**(17), 173901 (2017).

63. S. A. H. Gangaraj, G. W. Hanson, and M. Antezza, "Robust entanglement with three-dimensional nonreciprocal photonic topological insulators," Phys. Rev. A **95**(6), 063807 (2017).

64. A. Ghanekar, L. Lin, and Y. Zheng, "Novel and efficient mie-metamaterial thermal emitter for thermophotovoltaic systems," Opt. Express **24**(10), A868 (2016).

65. Y. Tian, X. Liu, A. Ghanekar, F. Chen, A. Caratenuto, and Y. Zheng, "Blackbody-cavity ideal absorbers for solar energy harvesting," Sci. Rep. **10**(1), 20304 (2020).

66. Z. M. Zhang, X. Wu, and C. Fu, "Validity of kirchhoff's law for semitransparent films made of anisotropic materials," J. Quant. Spectrosc. Radiat. Transfer **245**, 106904 (2020).

67. L. Zhu and S. Fan, "Near-complete violation of detailed balance in thermal radiation," Phys. Rev. B **90**(22), 220301 (2014).

68. B. Zhao, Y. Shi, J. Wang, Z. Zhao, N. Zhao, and S. Fan, "Near-complete violation of kirchhoff's law of thermal radiation with a 0.3 t magnetic field," Opt. Lett. **44**(17), 4203–4206 (2019).

69. D. A. B. Miller, L. Zhu, and S. Fan, "Universal modal radiation laws for all thermal emitters," Proc. Natl. Acad. Sci. U. S. A. **114**(17), 4336–4341 (2017).

70. Z. M. Zhang, "Rigorous coupled-wave analysis (rcwa)," http://zhang-nano.gatech.edu/Rad_Pro.htm. Accessed: 2021-03-15.

71. L. Wang and Z. M. Zhang, "Effect of magnetic polaritons on the radiative properties of double-layer nanoslit arrays," J. Opt. Soc. Am. B **27**(12), 2595–2604 (2010).

72. B. J. Lee, Y. B. Chen, and Z. M. Zhang, "Transmission enhancement through nanoscale metallic slit arrays from the visible to mid-infrared," J. Comput. Theor. Nanosci. **5**(2), 201–213 (2008).

73. M. Foldyna, K. Postava, D. Ciprian, and J. Pistora, "Modeling of magneto-optical properties of lamellar nanogratings," J. Alloys Compd. **434-435**, 581–583 (2007).

74. X. Luo, M. Zhou, J. Liu, T. Qiu, and Z. Yu, "Magneto-optical metamaterials with extraordinarily strong magneto-optical effect," Appl. Phys. Lett. **108**(13), 131104 (2016).

75. V. V. Temnov, I. Razdolski, T. Pezeril, D. Makarov, D. Seletskiy, A. Melnikov, and K. A. Nelson, "Towards the nonlinear acousto-magnetoplasmonics," J. Opt. **18**(9), 093002 (2016).

76. B. Sepulveda, J. B. Gonzalez-Diaz, A. Garcia-Martin, L. M. Lechuga, and G. Armelles, "Plasmon-induced magneto-optical activity in nanosized gold disks," Phys. Rev. Lett. **104**(14), 147401 (2010).

77. M. A. Ordal, R. J. Bell, R. W. Alexander, L. A. Newquist, and M. R. Querry, "Optical properties of al, fe, ti, ta, w, and mo at submillimeter wavelengths," Appl. Opt. **27**(6), 1203–1209 (1988).

78. E. D. Palik, R. Kaplan, R. W. Gammon, H. Kaplan, R. F. Wallis, and J. J. Quinn, "Coupled surface magnetoplasmon-optic-phonon polariton modes on insb," Phys. Rev. B **13**(6), 2497–2506 (1976).

79. Z. Q. Qiu and S. D. Bader, "Surface magneto-optic kerr effect," Rev. Sci. Instrum. **71**(3), 1243–1255 (2000).

80. D. W. Ball, "Wien's displacement law as a function of frequency," J. Chem. Educ. **90**(9), 1250–1252 (2013).

81. A. P. Ayala, "Polymorphism in drugs investigated by low wavenumber raman scattering," Vib. Spectrosc. **45**(2), 112–116 (2007).

82. *A Practical Schottky Mixer for 5 THz (Part II)* (Seventh International Symposium on Space Terahertz Technology, Charlottesville, 1996).